CO_2 Conversion Performance of Perovskite Oxides Designed with Abundant Metals

Bryan J. Hare[a], Debtanu Maiti[a], Anne J Meier[a,b], Venkat R. Bhethanabotla, [a] and John N. Kuhn[a*]*
Department of Chemical & Biomedical Engineering
University of South Florida
Tampa, FL 33620 USA
Email: jnkuhn@usf.edu, bhethana@usf.edu

[a] Department of Chemical & Biomolecular Engineering, University of South Florida, Tampa, FL 33620, USA.
[b] Analytical Laboratories Branch, NASA Kennedy Space Center, FL 32899, USA. Mail Stop NE-L3.

Abstract

With improved technology, CO_2 could be the feedstock for production of renewable fuels. The reverse water-gas shift chemical looping (RWGS-CL) process performs at lower temperatures and higher energy efficiencies than rival methods. Ideal materials must endure reaction conditions, exhibit high activity, and be synthesized from readily available elements. Design and characterization of $La_xCa_{1-x}Fe_yMn_{1-y}O_3$ perovskite-type oxides resulted in higher CO yields and peak formation rates than previously witnessed in RWGS-CL. Extents of Ca-/Fe-doping presented strong effects on lattice stability (XRD), conversion temperatures, and CO formation (TPO-CO_2). Samples calcined at higher temperatures exhibited greater stability and activity but higher conversion temperatures. Vacancy formation energies (DFT), decreased significantly and slightly with increasing Ca and Fe content, respectively, to reflect experimental findings. Surface allocation of metals suggest Fe is redistributed to the surface (XPS) for intensified CO_2 conversion with Mn-rich bulk for enhanced oxygen storage capacity and intralattice diffusion.

1. Introduction

An increasing concentration of atmospheric carbon forewarns mankind of irreversible consequences and tasks engineers to establish technologies for renewable energy production. As estimated by the U.S. Energy Information Administration, total national CO_2 emissions summed up to ~5.2 GT in 2017[1] while use of renewables consisted of a mere 12.7% of all energy consumption.[2] Even with the progressive adoption of alternative conversion and storage processes (Wind, solar, etc), the demand for energy continues to escalate while the reliance of high capacity transportation systems on conventional carbon-based fuels remains. By reducing CO_2 to CO, an essential component of synthesis gas, using available solar-to-fuels technology,[3,4] society can achieve feasible production of a variety of energy-dense chemicals including hydrocarbons, alcohols, and dimethyl ether.[5-7] This technique would also prove beneficial for NASA's mission to extend mankind's jurisdiction to Mars. The atmospheric processing module (APM) is designed to cryogenically captures CO_2 (~95 % of the Martian atmosphere) prior to CH_4 propellant formation through the Sabatier reaction.[8-10] CO_2 conversion to CO would permit downstream storable liquid fuel production using excess carbon that is otherwise wasted; i.e. CH_4 is emitted to achieve the desired O_2:CH_4 fuel ratio.[11,12] Worlds powered by carbon neutral (or zero) energy sources have the potential to sustain high standards for clean and efficient energy.

The reverse water-gas shift chemical looping (RWGS-CL) process is a simple 2-step low energy thermochemical reaction (typically 450 – 750 °C) that involves the sequential flow of H_2 and CO_2 to produce H_2O and CO separately and respectively with exceptional selectivity.[13-15] The conventional reverse water-gas shift was shown to demonstrate notable efficiency and

high leverage when operating concurrently with the Sabatier reaction and is capable improving APM carbon efficiency.[11,12] Furthermore, Wenzel and Rihko-Struckmann demonstrated much greater energy efficiencies for chemical looping processes with respect to their temperature swing counterparts; as high as 54% less energy consumption for the RWGS-CL process.[16] The use of a parallel reactor system or circulating fluidized bed[17] will ensure quick CO_2 conversion cycles to alleviate concerns of a low equilibrium constant.[18,19] With current technology and improving materials, the RWGS-CL process is capable of coexisting with the APM **(Figure 1)** for enhanced resourcefulness.

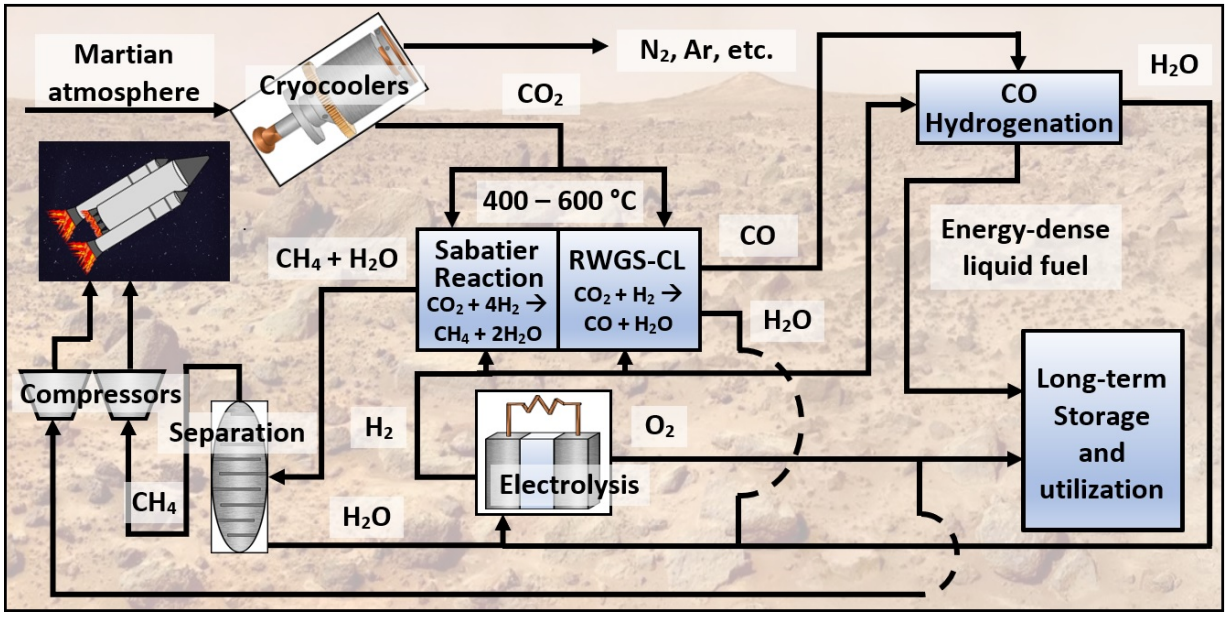

Figure 1. Modified atmospheric processing module with reverse water-gas shift chemical looping

Efficient RWGS-CL is contingent on the use of metal oxide catalysts that retain stability over numerous cycles.[13] A suitable catalytic material should be comprised of elements obtained from in-situ resource utilization and maintain adequate resistance to phase changes or decomposition. The oxide is first exposed to pure H_2 during the first half-reaction to initiate

partial reduction and form oxygen vacancies. These vacancies suffice as active sites for CO_2 conversion to CO during the latter step of the process when the original oxygen stoichiometry is replenished. As a simple binary oxide, CeO_2 has demonstrated exceptional redox activity during thermochemical CO_2/H_2O splitting[20,21] and was implemented into heat-recovering solar flux generators.[3,22] However, Ce is a scarce element, not yet discovered on Mars, thus shifting attention to more practical alternatives. Martian regolith consists of Fe oxide species[23] that can convert CO_2 at impressively low temperatures, 450 – 550 °C (or as high as 1400 °C for thermochemical splitting), yet struggle to achieve notable CO production rates and peak conversion efficiencies without existing concurrently with expensive supports such as CeO_2 or Y-stabilized ZrO_2.[24-26] Thus, perovskite-type oxide catalysts can serve as the primary candidate materials for feasible CO_2 conversion on both Earth and Mars. Perovskites retain body-centered structures surrounded by tetrahedral vertices to establish the distinctive ABO_3 empirical formula. The A-site often consists of lanthanides and alkaline earth metals while the latter B-site is typically comprised of transition metals and possibly semimetals.[27] By tailoring sites with different metals, scientists have access to a virtually unbounded range of perovskite materials that may be synthesized and tested for a wide variety of applications.[28] For example, lanthanide-based perovskites may be doped with more abundant elements to tune essential parameters such as structural stability, oxygen capacity, vacancy formation temperatures, and CO_2 convertability.[29] By synthesizing a perovskite based on elements both abundant on Earth and discovered on Mars, researchers may develop a material and further optimize CO_2 to CO conversion.

$LaFeO_3$, and several doped variations, has recently shown promising results for CO_2 conversion and a variety of other redox applications.[15,30-36] La is essential for maintaining high structural stability and thermal endurance.[27] Although it is yet to be discovered on Mars, its utilization can still be reduced through tailoring of the A-site. Ca-doped perovskites were recently proved, both computationally and experimentally, to demonstrate higher activity for CO_2 conversion than traditional Sr- and Ba-doped alternatives.[29] This is due to optimal oxygen vacancy formation energies (~3.4 eV) and higher oxygen self-diffusion coefficients.[29,37] In addition, Mn-based perovskites demonstrate large oxygen carrying and uncoupling capacities which suggest they can significantly increase CO_2 conversion sites and yields.[38-40] This oxygen hyper-stoichiometry is furthered enlarged with the substitution of small A-site cations which facilitate a significant extent of trivalent to tetravalent Mn transition.[41] Fortunately, large deposits of both Ca- and Mn-based compounds were recently discovered in proximity to the Gale Crater and Phoenix Landing Site.[42-44] This leaves mankind with many of the basic resources necessary to develop a Mars-abundant catalyst for feasible CO_2 to CO conversion.

The focus of this project is the synthesis, characterization, and reaction testing of the $La_{1-x}Ca_xFe_{1-y}Mn_yO_3$ perovskite-type oxide, a material comprised of elements abundant on both Earth and Mars. The optimal extents of A- and B-site doping were determined by observed secondary phase formation and density functional theory-based calculations to predict structural stability and oxygen vacancy formation energies, respectively. X-ray diffraction confirmed adequate stability for top-performing samples following temperature-programmed experiments. X-ray photoelectron spectroscopy provided insight to intracrystalline migration of cations and changes in surface composition following experiments.

2. Methods

2.1. Synthesis

The $La_{1-x}Ca_xFe_{1-y}Mn_yO_3$ perovskites (x = 0.25, 0.50, 0.75 and y = 1.0, 0.75, 0.50) were synthesized via a gel-based Pechini method.[45,46] This particular method permits relatively quick acquisition of a wide array of different compositions. It should be noted that for the sake of feasible ISRU on Mars, the optimized CO_2 redox catalyst would be synthesized via solid-state sintering of binary oxide or hydroxide precursors, thus requiring more time and higher temperatures.[47] The ranges for Ca- and Mn-doping were decided based on Goldschmidt tolerance factor calculations and previous work done by Coates and McMillan.[48] We observed in our study that doping perovskites with high Ca-content with over 50% Fe on the B-site results in the formation of a $Ca_2Fe_2O_5$ phase. Synthesis precursors consisted of metal nitrate and carbonates (Aldrich 99.9% $La(NO_3)_3$, Aldrich ACS grade +98% $Fe(NO_3)_3$) dissolved into a 2 M aqueous citric acid solution.[29,46] Following 2 hr of stirring to ensure minimal spatial variations, ethylene glycol was administered to initiate polyesterification which was sustained at 90 °C for 7 hr. The viscous gel was charred at 450 °C for 2 hr and then crushed into a fine powder. Samples were finally calcined for 6 hr at either 950 °C, as previously conducted,[29] or 1200 °C to further improve crystalline stability.

2.2. Temperature-programmed experiments

Temperature-programmed experiments were performed to test the vacancy formation and CO_2 conversion capabilities of the $La_{1-x}Ca_xFe_{1-y}Mn_yO_3$ perovskite. A Cirrus MKS mass spectrometer was used to monitor the effluent of a quartz microreactor that employed about

75 mg of sample. Ultra high purity helium from Airgas served as a carrier gas for a total flow rate of 50 sccm. Temperature-programmed reductions (TPR) consisted of a 10% H_2/He (v/v) flow as the sample was heated up to 950 °C at a 10 °C/min heating rate. Temperature programmed oxidations (TPO-CO_2) began with a 30 min isothermal reduction of the sample at 600 °C in 10% H_2/He (v/v). The reduced material was cooled naturally in 100% He to maintain vacancies prior to the oxidation step. The flow was switched to 10% CO_2/He (v/v) and the temperature was ramped to 950 °C at 10 °C/min, hence producing quantifiable CO.

2.3. Characterization

Crystallographic data from X-ray diffraction (XRD) was used to determine the lattice geometry and parameters of LCFM. Diffraction patterns were acquired using a Bruker X-Ray Diffractometer with a Cu Kα and a wavelength (λ) of 1.54 nm. Miller indices were indexed using data from similar crystal structures[49,50] while the least squares sum method was used to obtain lattice parameters a, b, and c along with the corresponding cell volume.

Catalyst surfaces were probed using X-ray photoelectron spectroscopy and N_2-physisorption. A Thermo Scientific Kα instrument was used to measure atomic surface composition and with a C 1s peak located at ~285.2 eV. A Quantachrome Autosorb IQ analyzer was utilized to adsorb N_2 to the oxides at 77 K, following degassing at 300 °C. The BET method was used to calculate specific surface areas using isotherm data points in the range of $0.05 < P/P_0 < 0.3$.

2.4. Density-functional theory (DFT)

The oxygen vacancy formation energies were calculated by spin-polarized density functional theory (DFT) calculations using Vienna ab-initio simulation package (VASP-5.3.3).[51-55]

Plane wave basis sets were used for all the calculations and the electron densities were approximated by generalized gradient approach (GGA). Projector augmented wave (PAW) potentials[54] and the Perdew-Burke-Ernzerhof (PBE)[56] variant of exchange-correlations were used throughout the calculations, with a consistent 600 eV energy cutoff. A 4 × 4 × 4 *k*-point mesh having a Monkhorst pack grid[57] was used to probe the 2 × 2 × 2 supercell consisting of 40 atoms of perovskite oxides. Stable stoichiometric configurations were obtained through energy-minimization of several different configurations. The oxygen deficient materials were created by removing an oxygen atom from these 40-atom supercells and the oxygen vacancy formation energy was calculated as per the following equation:

$$E_{vac} = E_{ABO_{(3-\delta)}} + n \times \frac{\delta}{2} E_{O_2} - E_{ABO_3} \qquad \textbf{(Eqn 1)}$$

where, E_{vac} is the vacancy formation energy to remove δ extent of oxygen vacancy. E_{ABO_3} is the energy of the pure stoichiometric phase, $E_{ABO_{(3-\delta)}}$ is that of the oxygen deficient material and n is the number of the unit cells. Since these mixed metal oxides present several oxygen sites (i.e. diverse combinations of AO and BO_2 terminations), and thus, several different energy values, we report oxygen vacancy formation energies averaged over these different sites. The oxygen over-binding error has been accounted for as well.[58]

Results

Temperature-programmed experiments

The RWGS-CL process consists of two half-reactions carried out separately. The first step is H_2-induced formation of oxygen vacancies (Rxn 1); those of which on the surface serve as active sites for CO_2 conversion.

$$H_2 + ABO_3 \rightarrow H_2O + ABO_{3-\delta} \qquad \textbf{(Rxn 1)}$$

The δ term represents the extent of oxygen vacancy formation (quantified during isothermal reduction step of TPO-CO_2 experiments). The latter half reaction (Rxn 2) is the actual conversion of CO_2 to CO through replenishment of these oxygen vacancies.

$$CO_2 + ABO_{3-\delta} \rightarrow CO + ABO_3 \qquad \textbf{(Rxn 2)}$$

C-O bond cleavage occurs on oxygen-deprived surface facets and the resulting oxygen anion diffuses within the bulk until a sufficient amount of oxygen is reacquired. The precise composition of these perovskite materials is expected to demonstrate profound effects on reaction efficacies and material stability.

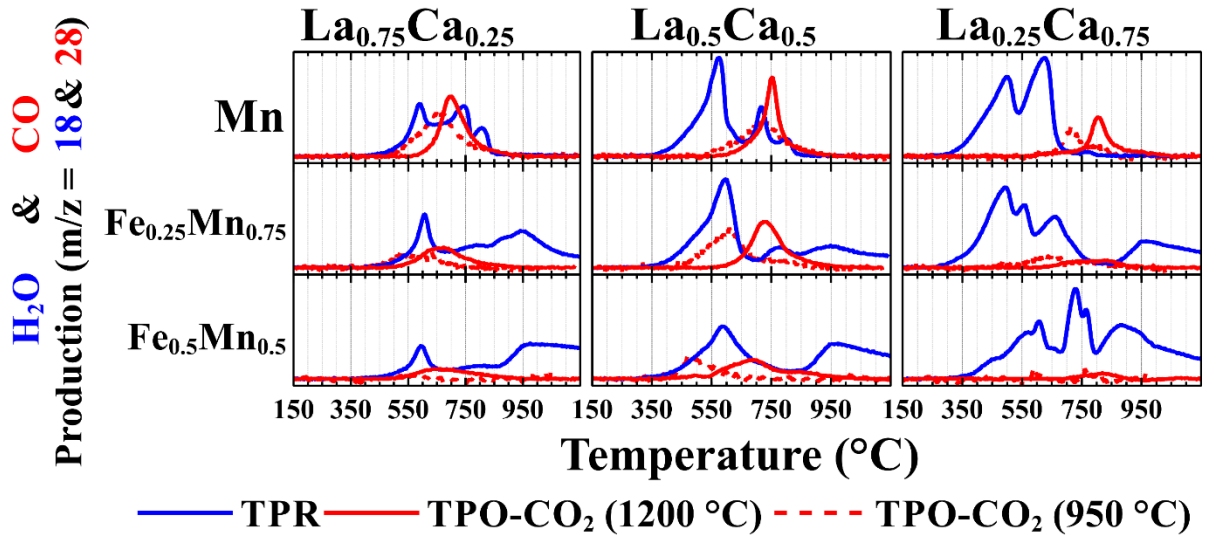

Figure 2. Temperature-programmed reduction (with H_2) and oxidation (with CO_2) profiles

Table 1. H_2O production during isothermal reduction period (30 min at 600 °C under 10% (v/v) H_2/He) of TPO-CO_2 experiments. For each LCFM species, H_2O data is organized as "mmol H_2O/g_{cat} (δ)." δ represents the extent of oxygen vacancy formation in ABO_3 species.

Calcination temp.		**$La_{0.75}Ca_{0.25}$**	**$La_{0.5}Ca_{0.5}$**	**$La_{0.25}Ca_{0.75}$**
950 °C	**Mn**	2.65 (0.58)	3.33 (0.64)	4.59 (0.88)
1200 °C		1.89 (0.41)	2.90 (0.56)	5.05 (0.85)
950 °C	**$Fe_{0.25}Mn_{0.75}$**	1.61 (0.35)	2.90 (0.56)	4.07 (0.68)
1200 °C		1.23 (0.27)	2.67 (0.52)	3.71 (0.62)
950 °C	**$Fe_{0.5}Mn_{0.5}$**	1.33 (0.29)	2.13 (0.35)	2.57 (0.43)
1200 °C		0.87 (0.19)	2.14 (0.41)	2.48 (0.42)

Reaction products were monitored and quantified over a temperature span from ambient conditions to 950 °C. Temperature-programmed reaction profiles **(Figure 2)** reveal the thermodynamic conditions for both onset and peak rate formation of H_2O and CO. The majority of LCFM perovskites demonstrated a reduction onset temperature of about 350 °C similar to that of other previously tested materials such as $La_{0.75}Sr_{0.25}FeO_3$.[15] The amount of H_2O produced **(Table 1)** is directly related to the extent of vacancy formation (δ), and therefore, the number of active sites for CO_2 conversion. With C-O bond cleavage occurring at oxygen-deprived surface facets, each vacancy is expected to accommodate the oxygen produced from dissociating a single CO_2 molecule. However, the CO_2 yields fall short of H_2O production which further support the theory of kinetic stagnation in oxide catalysis, previously suggested by DFT.[59] As the oxygen-vacant bulk continues to replenish its stoichiometry, the material's

willingness to further oxidize decreases. This intuitively denotes the permanent removal of surface oxygen that does not inherently contribute to the intrinsic oxygen stoichiometry in ABO_3 species. In a RWGS-CL application, this phenomenon would result in a slight decrease in catalytic activity after the initial cycle as witnessed beforehand.[15]

Table 2. CO production and rate quantifications during oxidation period (up to 950 °C in 10% (v/v) CO_2/He) of TPO-CO_2 experiments. For each LCFM species, CO data is organized as "mmol CO/g_{cat} (peak mmol CO/g_{cat}/min, corresponding temperature)"

Calcination temp.		**$La_{0.75}Ca_{0.25}$**	**$La_{0.5}Ca_{0.5}$**	**$La_{0.25}Ca_{0.75}$**
950 °C	**Mn**	1.68 (0.10, 660 °C)$^{\alpha}$	1.39 (0.09, 720 °C)$^{\alpha}$	0.67 (0.07, 720 °C)$^{\alpha}$
1200 °C		1.59 (0.14, 690 °C)	1.45 (0.18, 750 °C)	0.91 (0.09, 800 °C)$^{\alpha}$
950 °C	**$Fe_{0.25}Mn_{0.75}$**	0.53 (0.03, 640 °C)	1.38 (0.09, 610 °C)	0.47 (0.03, 640 °C)$^{\alpha}$
1200 °C		0.84 (0.05, 670 °C)	1.45 (0.11, 720 °C)	0.33 (0.02, 830 °C)$^{\alpha}$
950 °C	**$Fe_{0.5}Mn_{0.5}$**	N.D.$^{\beta}$	0.53 (0.06, 470 °C)	N.D.$^{\beta}$
1200 °C		0.52 (0.02, 640 °C)	0.86 (0.04, 690 °C)	0.01 (0.01, 810 °C)$^{\alpha}$

$^{\alpha}$Phase deformation witnessed in post TPO-CO2 XRD
$^{\beta}$None detected

Reaction data in **Tables 1 and 2** suggest that samples of higher Mn content result in both greater rates and yields of CO. In particular, the $La_{0.5}Ca_{0.5}MnO_3$ (1200 °C) species demonstrated a rate of 0.18 mmol CO/g_{cat}/min with a total production of 1.45 mmol CO/g_{cat}. One vital drawback of this material, and others of similar composition, is higher conversion temperatures. While this concern may be somewhat alleviated by incorporation of Fe into the lattice, average CO yields and rates are consequentially affected. $La_{0.5}Ca_{0.5}Fe_{0.25}Mn_{0.75}O_3$,

however, appears to be a slight exception; which maintained CO yields around 1.45 mmol CO/g_{cat}. These results are directly compared to those of Sr-based redox materials **(Table 3)**.

Table 3. CO_2 to CO conversion performance by Sr-doped perovskite alternatives

Species	CO yield ($mmol/g_{cat}$)	CO formation rate ($mmol/g_{cat}/min$)	Notes	Reference
$La_{0.75}Sr_{0.25}CoO_3$	0.23	0.19	RWGS-CL (Reduced at 600 °C, CO rate measured at 850 °C)	[13]
$La_{0.6}Sr_{0.4}Mn_{0.6}Al_{0.4}O_3$	0.17	-	CO_2 splitting at > 1000 °C	[60]
$La_{0.5}Sr_{0.5}MnO_3$	0.13	-	CO_2 splitting at 1400 °C under P_{CO_2} of 1 atm	[61]
$La_{0.5}Sr_{0.5}Mn_{0.5}Fe_{0.5}O_3$	0.14	0.05	CO_2 splitting at 1400 °C P_{CO_2} of 0.5 atm	[62]
$La_{0.5}Ca_{0.5}MnO_3$	1.45	0.19	From this study	-

As with those of the aforementioned species, perovskites capable of efficient cyclic redox reactions often display an initial large reduction peak, representing the formation of surface and bulk vacancies. This is then followed by a smaller and broader reduction peak that depicts the concomitant desorption of more oxygen and deconstruction of the perovskite into binary oxides. For samples with high La content ($La_{0.75}Ca_{0.25}BO_3$), the partial reduction peak is relatively small and corroborates the smaller overall CO yields. $La_{0.75}Ca_{0.25}MnO_3$, calcined at either 950 or 1200 °C, remains an exception possessing the highest CO yields of the matrix. While this extent of La content is not ideal for ISRU, doping this species with Fe in an attempt to reduce conversion temperature leads to a significant reduction in both CO yield and rate. On the other hand, samples with high Ca content exhibit reduction profiles with an ambiguous assembly of peaks. This may denote the material's inability to sustain an oxygen vacant lattice

as well as a multitude of phase changes occurring prior to the favored formation of binary oxides.

Lattice Properties and Stability

Innate stability of each LCFM combination is generally predetermined by the Goldschmidt tolerance factor. Cherry et al. proposed a factor range of $0.75 < t < 1.0$ for perovskite-type oxides. Any sample synthesized with $y < 0.5$ (over 50% Fe on the B-site) contained a significant amount of $Ca_2Fe_2O_5$. Slight formation of La_2O_6 was also noted after synthesizing $LaMnO_3$. Having witnessed several phase changes following TPO-CO_2 experiments, it is equitable to state that La-based ferrites, such as $La_{0.75}Sr_{0.25}FeO_3$, are more structurally sound.[14,15,63] Nonetheless, compositional trends for stability or phase changed are evident in the diffraction patterns **(Figure 3)** and several LCFM perovskites within the range of stability accommodated with much larger CO yields. For samples that experienced a major phase change, the same aforementioned impurity phases became much more prominent. The main (200) diffraction line remained firm or shifted leftwards for all other samples depicting an increase in the lattice volume. This thermodynamic response may account for the material's accommodation for larger bulk oxygen fluxes, represent a step towards decomposition that may occur after multiple cycles, or a combination thereof.

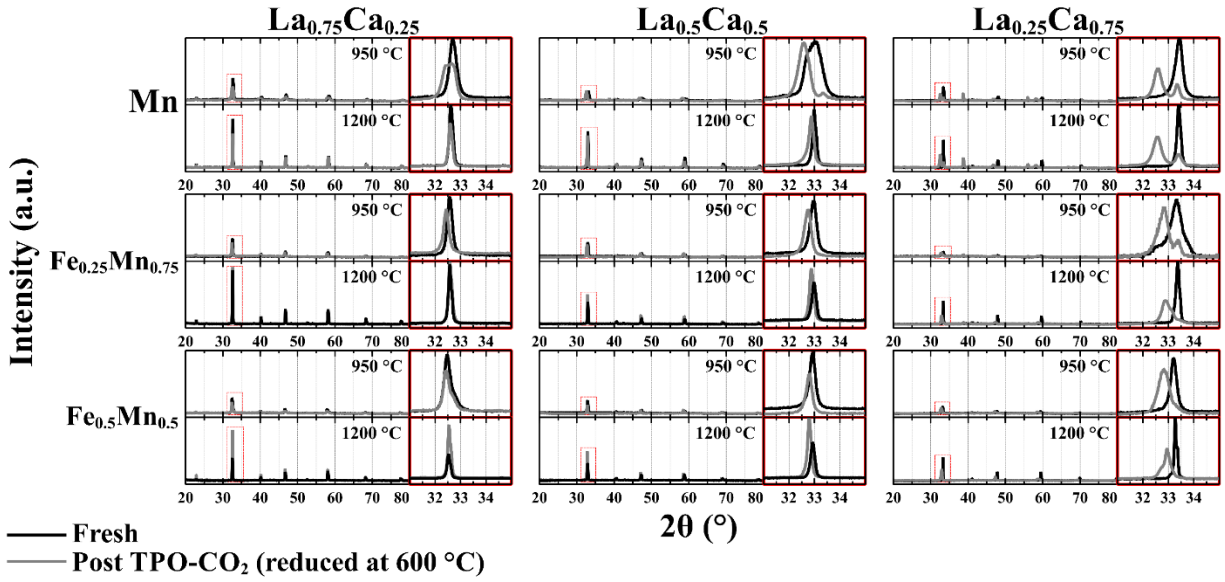

Figure 3. XRD patterns of the LCFM perovskites before and after TPO-CO_2 experiments. The right portion of each plot is a zoomed in image of the main diffraction line located at 32-34 2θ.

Table 4. Cell volumes (Å^3) of LCFM calcined at 950 °C (top) and 1200 °C (bottom).

Calcination temp.		$La_{0.75}Ca_{0.25}$	$La_{0.5}Ca_{0.5}$	$La_{0.25}Ca_{0.75}$
950 °C	**Mn**	230.96	228.71	216.34
1200 °C		232.18	225.38	219.17
950 °C	**$Fe_{0.25}Mn_{0.75}$**	233.49	225.81	218.36
1200 °C		231.77	225.63	217.58
950 °C	**$Fe_{0.5}Mn_{0.5}$**	235.33	226.40	220.53
1200 °C		232.38	225.50	219.19[α]

[α]Primary diffraction line is (002) instead of (200)

The resulting trends witnessed in relation to structural stability may also delineate the differences in CO formation rates between samples calcined at 950 °C and 1200 °C. Normally, one may expect faster oxygen migration through larger lattice volumes.[64,65] The orthorhombic lattice volumes of LCFM **(Table 4)** show a clear trend of decreasing volume with increasing Ca content. However, the highest CO formation rates observed in this study correspond primarily with $La_{0.5}Ca_{0.5}BO_3$ species. Previous theories state that smaller A-site metals, larger B-site metals, and larger overall lattice volumes reflect the lowest oxygen migration energies and highest oxygen conductivities.[66] While in practice this would expectedly correspond with $La_{0.25}Ca_{0.75}BO_3$ species, the diffraction patterns explicitly reveal degradation of the perovskite phases. The extent of vacancy formation in these reaction conditions is too high for samples of high Ca-content to maintain a stable oxygen vacant structure. While this initially appears to contrast previous literature, the larger Full Width Half Maximum of the average $La_{0.5}Ca_{0.5}BO_3$ sample suggests a dissimilar distribution of A and B metals between the surface and bulk (i.e. a possible Ca-rich surface and La-rich bulk). A slight decrease in these lattice volumes was observed for the vast majority of samples when calcined at the latter temperature which in addition resulted in higher CO production rates.

Oxygen Vacancy Formation Energies

By utilizing DFT, a distinct trend was revealed relating atomic energetics to the intrinsic ability of a material to exhibit oxygen vacancies. Such trends of surface oxygen vacancy formation energies are largely dependent on the exact surface termination stability, elemental composition, surface reconstruction and strain. We have previously shown that oxygen vacancy formation energies

along the 'BO_2' terminations follow the same trends as the bulk.[59] However, we do note that these trends are extremely case-specific and are purely determined by the surface atoms, concentration, coordination, magnetic states and finally their oxidation states. The calculated E_{vac} for each LCFM perovskite **(Figure 4)** illustrates a significant decrease in E_{vac} with the introduction of Ca into the A-site and slight decrease with increasing Fe-doping within the B-site. However, the lowest E_{vac} does not correlate with the highest CO yield or rate. We previously demonstrated the swift change in redox activity of perovskites through Cu-doping which resulted in E_{vac} as low as 2.8 eV.[63] While this material readily formed vacancies upon exposure to hydrogen, similarly to

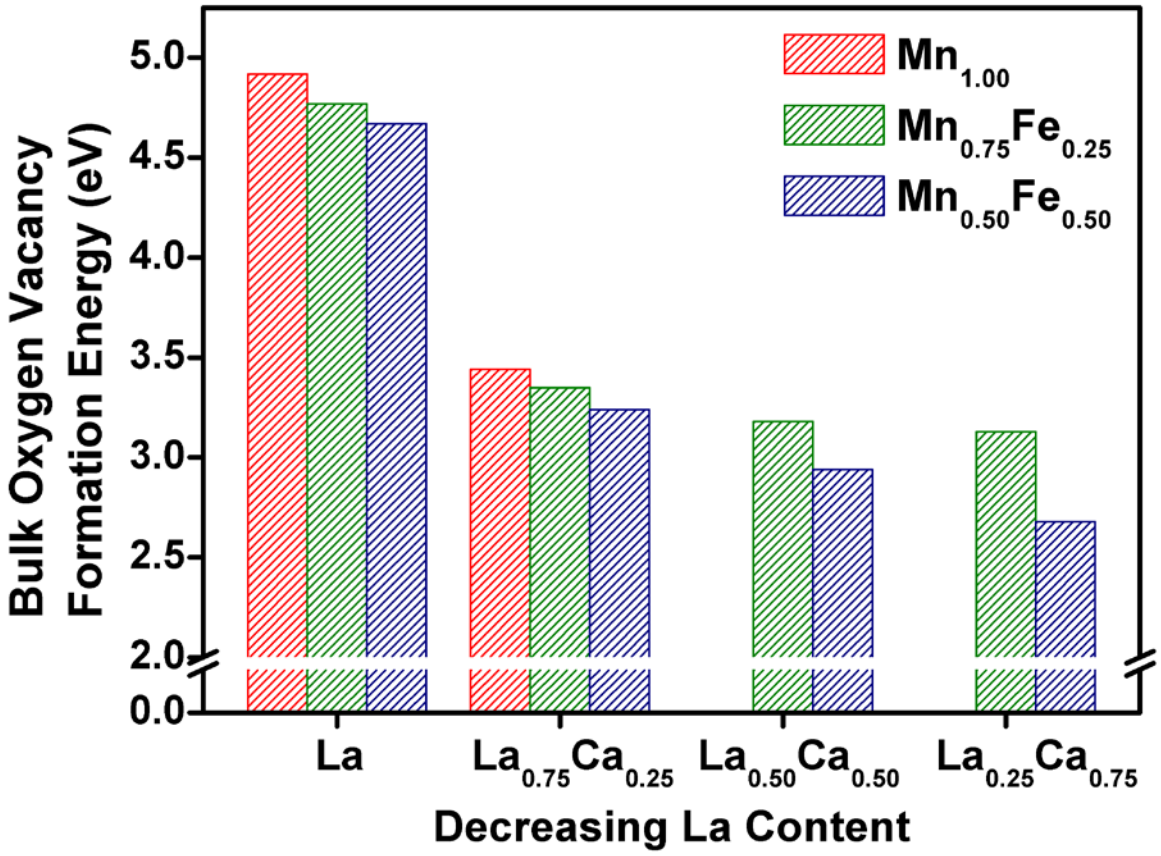

Figure 4. DFT-calculated oxygen vacancy formation energies (E_{vac}) for $La_{1-x}Ca_xFe_{1-y}Mn_yO_3$ (x = 0, 0.25, 0.5, 0.75 and y = 0.5, 0.75, 1.0)

$La_{0.25}Ca_{0.75}Fe_{1-y}Mn_yO_3$ (E_{vac} = ~2.6-3.1 eV), it kinetically refused uptake of oxygen through C-O bond cleavage and deconstructed into binary oxides. Species with high E_{vac}, such as $LaFe_{1-y}Mn_yO_3$ (E_{vac} = ~4.6-4.9 eV) will present less vacancy formation prior to decomposition, a higher onset reduction temperature, or simply no observable vacancy formation. Our ideal energy zone for CO_2 remains in the vicinity of about 3.36 ± 0.5 eV;[29] this covers many of the high performing samples including $La_{0.75}Ca_{0.25}MnO_3$, $La_{0.5}Ca_{0.5}MnO_3$, and $La_{0.5}Ca_{0.5}Fe_{0.25}Mn_{0.75}O_3$. Because the thermodynamic requirements to create bulk vacancies are similar, these materials are expected to convert notable quantities of CO_2 as confirmed by the TPO-CO_2 profiles.

While we have demonstrated both experimentally and computationally the efficacy of the LCFM perovskite for CO_2 conversion, performance endurance of these materials for extended chemical looping is also important. Aside from structural stability probed by XRD, it is essential for these materials to maintain the production rates witnessed in this study. Crystallite dimensions and oxygen migration energies may serve as descriptors for high H_2O and CO formation rates. Given that small particles are maintained, the rate of bulk-to-surface movement of lattice oxygen is expected to increase due to a smaller migration pathway and, therefore, reduced mass transport limitations.[15,67,68] The actual oxygen migration energy is determined by a multitude of factors but follows explicit trends regarding atomic composition. In the presence of a neighboring vacancy, the energy required to transfer across BO_6 octahedra generally decreases with smaller A-site cations (Ca^{2+} vs La^{3+}) and larger B-site cations ($Fe^{2+/3+}$ vs $Mn^{3+/4+}$).[66,69] According to DFT calculations and XRD patterns, an optimized composition is necessary to avoid low E_{vac} and lattice decomposition due to excess Ca-content.

Table 4. BET surface areas (m^2/g) of LCFM calcined at 950 °C

	$La_{0.75}Ca_{0.25}$	$La_{0.5}Ca_{0.5}$	$La_{0.25}Ca_{0.75}$
Mn	4.6	5.9	4.6
$Fe_{0.25}Mn_{0.75}$	4.0	7.4	4.3
$Fe_{0.5}Mn_{0.5}$	3.7	5.0	4.4

Surface Characterization

It is important to study the surface of these materials where CO_2 is ultimately converted to CO. The LCFM material, and most other perovskite-type oxides in general, commonly exhibit low surface areas due to the high temperatures required for calcination and the assurance of a stable crystalline structure. All BET analyses of LCFM samples calcined at 950 °C **(Table 4)** resulted in surface areas below 10 m_2/g, similar to those in studies regarding the same materials.[70] These are expected to be somewhat lower for those calcined at 1200 °C. However, our group previously reversed this perovskite agglomeration and obtained nanoparticles with higher surface area by the addition of binary oxide supports; most notably SiO_2.[15,71] Larger surface area to volume ratios would not only increase CO_2 adsorption, and therefore conversion, but it also decreases the mass transfer resistance of self-diffusing oxygen given smaller intracrystalline diffusion pathways.

Perovskite bulk material is generally treated as a network of interconnected and atomically homogenous lattices. Differences in surface composition of $La_{0.5}Ca_{0.5}MnO_3$ and $La_{0.5}Ca_{0.5}Fe_{0.25}Mn_{0.75}O_3$ prior to and following exposure to TPO-CO_2 reaction conditions **(Figure 5)** however evidently suggest migration of metal cations and oxygen to form more thermodynamically favored facets. Each surface remains A-metal dominant, specifically due to

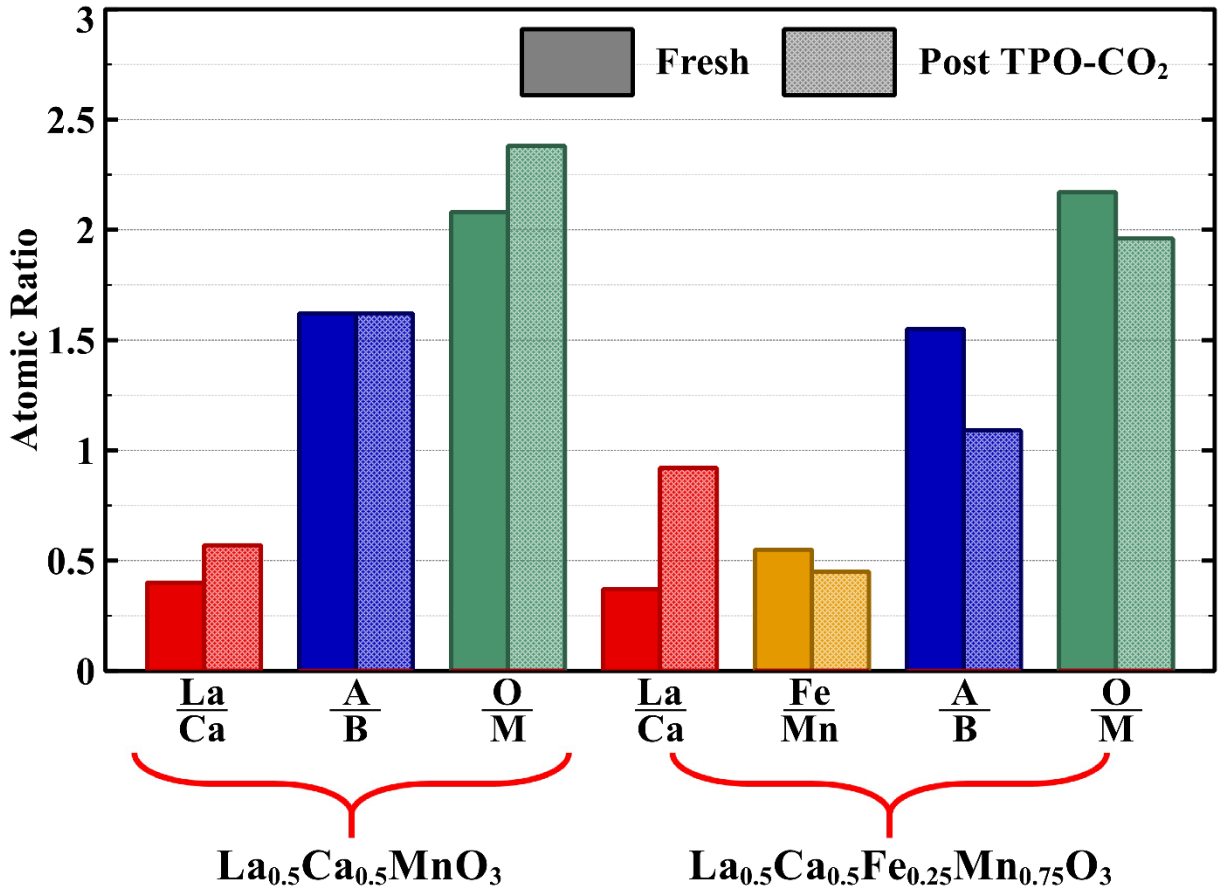

Figure 5. Surface compositions of fresh/post TPO-CO_2 LCM 50-50_100 and LCFM 50-50_25-75 calcined at 1200 °C. A/B represents perovskite constituents in ABO_3 and O/M represents the oxygen-to-metal ratio.

high Ca content in fresh samples. This is expected to reduce the mass transfer resistance of CO_2 to the perovskite surface. Contrary to previous studies that witnessed dopant enrichment on the surface of $La_{1-x}Sr_xBO_3$ perovskites,[72,73] there appears to be an inward flux of Ca, a phenomena previously witnessed by our group.[29] As supported by magnitude changes in the Ca 2p orbital spectra **(Figure 6b)**, the dopant retains dominance in AO surface terminations. The Ca $2p_{3/2}$ and $2p_{1/2}$ peaks, located at 347 and 351 eV respectively.[74] The primary La 3d multiplet was situated in the range of 832-840 eV and exhibited a slight increase in magnitude. The energy difference within the split was 4.3 eV suggesting the minute presence of metal carbonate

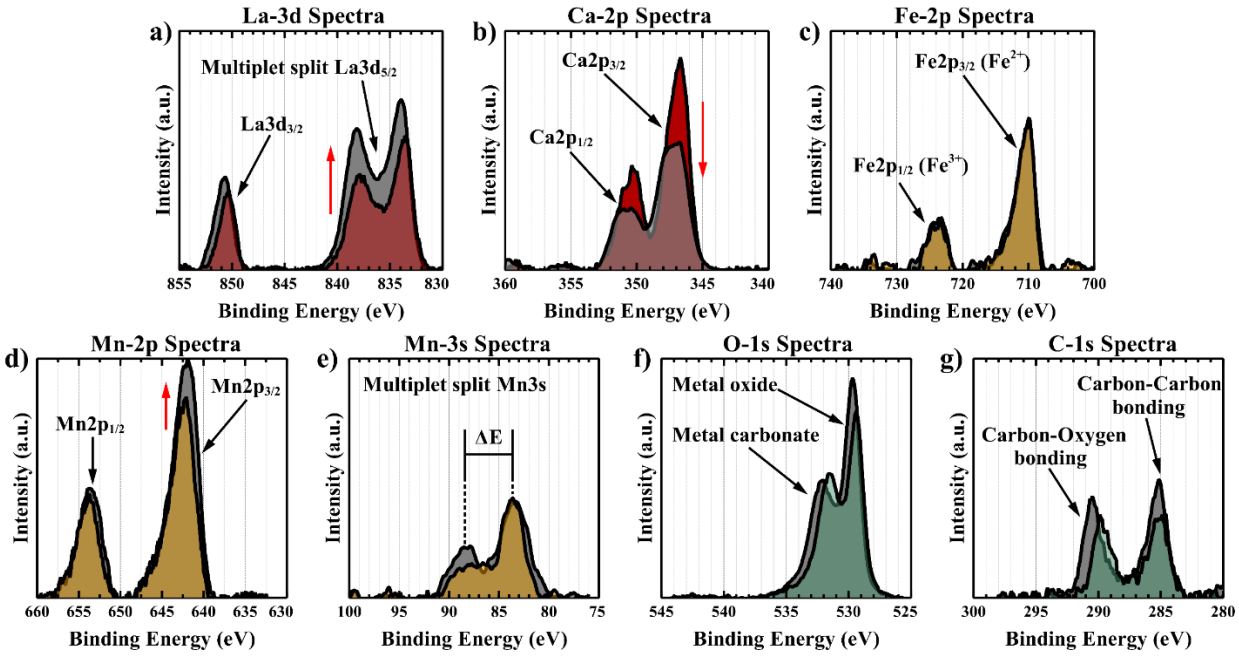

Figure 6. XPS spectra of the a) La-3d, b) Ca-2p, c) Fe-2p, d) Mn-2p, e) Mn-3s, f) O-1s, and g) C-1s orbitals in fresh (colored) and post TPO-CO_2 (gray) LCFM 50-50_25-75.

species, supported by the C 1s spectra.[74,75] It is likely that Ca diffusion is the initial step in A-site rearrangement due to a lower migration energy than that of La.[76] This phenomena is theoretically beneficial for the overall intrinsic performance of stable LCM and LCFM species. Oxygen self-diffusion (i.e. vacancy formation and replenishment) is expected to occur much quicker with increasing Ca bulk content.[37] In addition, the combination of La- and Ca oxide-based surface facets is expected to increase both CO_2 adsorption through improved stability and carbonate formation at higher temperatures as witnessed by CO_2 capture studies.[77]

A greater portion of the Fe dopant is allocated to the surface of $La_{0.5}Ca_{0.5}Fe_{0.25}Mn_{0.75}O_3$. This is due to the lower energy required for the Fe^{3+}/Fe^{2+} transition in comparison to Mn^{4+}/Mn^{3+}, proven by DFT calculations. XPS spectra of these transition metals **(Figure 6c-e)** provide insight to the valency distribution. As expected, the Fe 2p spectra ultimately includes a large peak at 710 eV for the $2p_{3/2}$ spin state accompanied by a smaller $2p_{1/2}$ peak at 722 eV.[74]

Although comparatively small, the presence of satellite peaks at 731.9 and 719.3 eV represent a mixture of divalent and trivalent Fe species. For Mn, XPS spectra was obtained for both the 2p and 3s orbitals, the latter of which depicts the average valency based on the ΔE measured within the multiplet split.[74] This binding energy difference was calculated to be ~5.2 eV for both fresh and post TPO-CO_2 which suggests a higher and seemingly unchanged concentration of Mn^{4+}. While it is generally known that incorporation of divalent A-site dopants forces a greater portion of Mn to the tetravalent state,[78] an excess of Ca must be avoided to ensure thermal endurance and stability of the perovskite used in these reaction conditions.

The average surface oxygen-to-metal ratios for both LCM and LCFM are relatively low compared to typical perovskite stoichiometry one would find within the bulk. This is due to the material's increasing reluctance to further consume oxidizing agents (O_2 or CO_2) as the vacant lattice is increasingly replenished, whether during synthesis or redox experiment.[14] It is important to note that the La/Ca ratio approaches unity following the TPO-CO_2 experiment with LCFM. This is likely an intrinsic propensity of the material to stabilize itself during a high rate of Ca migration in the presence of Fe. As aforementioned, perovskite structures are unobtainable with high Ca and Fe content. Samples that were unable to sustain a vacant lattice or safely reallocate Ca and Fe separately (i.e. $La_{0.25}Ca_{0.75}BO_3$) experienced partial decomposition into $Ca_2Fe_2O_5$ and concomitant formation of a La- and Mn-rich perovskite phase.

The O 1s spectra **(Figure 6f)** shows a strong peak at 530 eV representative of metal oxide surface species. However, the secondary peak at 532 eV suggests a notable metal carbonate presence and corroborates the carbon-oxygen binding peak in the C 1s spectra **(Figure 6g)** located at 290-291 eV.[74] Following high temperature exposure to CO_2 in

experiments, however, the slight 0.6 eV shift to a higher binding energy suggests an increasing surface concentration of lanthanum carbonates, most likely $La_2O_2CO_3$.[75,79,80] These species are known to thermally decompose above 700 °C yet with low conversions; even at small partial pressures of CO_2.[81] However, an assembly of Gibbs free energy calculations suggests that the oxidation of vacant perovskites by CO_2 is thermodynamically more favored at higher temperatures than carbonation of CaO facets into $CaCO_3$.[82-84] Our group previously showed CO formation rates in RWGS-CL at 600 °C are possibly hindered by these surface carbonates.[29] We suspect a low adsorption energy will reflect restrained CO_2 transfer to the surface while a high adsorption energy with result in the formation of strongly bonded A-metal carbonates that may not participate in the intended reaction. It may be of interest in future studies to delineate the effects of these species and calculate the optimal CO_2 adsorption energy required similar to the procedures done for E_{vac}.

Conclusion

This study synthesized, tested, and characterized an extensive matrix of $La_{1-x}Ca_xFe_{1-y}Mn_yO_3$ perovskites (x = 0.25, 0.50, 0.75 and y = 1.0, 0.75, 0.50) for CO_2 to CO conversion through the reverse water-gas shift chemical looping process. Perovskites calcined at 1200 °C generally exhibited greater structural stability (revealed by XRD), higher CO yields, and higher peak rates but 50-100 °C higher conversion temperatures (observed by TPR and TPO-CO_2 experiments). Total CO yields of stable, top-performing $La_{0.5}Ca_{0.5}MnO_3$ and $La_{0.5}Ca_{0.5}Fe_{0.25}Mn_{0.75}O_3$ calcined at 1200 °C were both 1.45 mmol CO/gcat and peak rates of 0.18 and 0.11 mmol CO/gcat/min respectively (up to 1.68 for $La_{0.75}Ca_{0.25}MnO_3$). These results

are much higher than those of popular Sr-doped alternatives. DFT-calculated oxygen vacancy formation energies of tested samples were calculated between 2.7 and 3.4 eV. The aforementioned perovskites exhibited E_{vac} values within the middle of this regime. Those with high E_{vac} (high La content) formed less vacancies and therefore fewer active sites for CO_2 conversion. Those with lower E_{vac} (high Ca content) experienced partial decomposition, often leaving behind a La- and Mn-rich perovskite phase and a secondary $Ca_2Fe_2O_5$ phase. The latter case maybe be due to unable stoichiometry and the material's inability to separately reallocate Ca and Fe during migration between the bulk and surface as probed by XPS. Further studies are required to delineate the effects of A-site carbonate species that are formed during oxidation by CO_2.

Conflicts of Interest

A provisional patent has been filed by USF on these materials and the reverse-water gas shift chemical looping process on behalf of B. J. H., D. M., V. R. B., and J.N.K. All systematic information regarding the Atmospheric Processing Module is the solely the intellectual property of the National Aeronautics and Space Administration. The authors do not claim ownership of the latter technology.

Acknowledgements

NSF grants IIP-1743623, CHE-1531590, and EEC-1560303, the NASA Florida Space Grant Consortium Masters Fellowship (to BJH), and the USF Office of Graduate Studies Dissertation Completion Fellowship (to DM) are gratefully acknowledged for funding. The authors would like

to recognize both the Kennedy Space Center (SAA) and Georgia Institute of Technology Materials Characterization facility for XPS data acquisition. Assistance with sample preparation, XPS probing, and BET analyses by Hanzhong Shi, Karoline Hebisch, and Adela Ramos, respectively, is heartily appreciated.

References

(1) Lindstrom, P. U.S. energy-related CO_2 emissions expected to rise slightly in 2018, remain flat in 2019. (U.S. Energy Information Administration, Washington D.C., 2018).
(2) U.S. Energy Facts Explained. (U.S. Energy Information Administration, Washington D.C., 2018).
(3) Furler, P., Scheffe, J. R. & Steinfeld, A. Syngas production by simultaneous spliting of H_2O and CO_2 via ceria redox reactions in a high-temperature solar reactor. *Energy Environ. Sci.* **2012**, *5*, 6098-6103.
(4) Ganesh, I. Conversion of carbon dioxide to methanol using solar energy. *Curr. Sci.* **2011**, *101*, 731-733.
(5) Sheldon, R. A. *Chemicals from Synthesis Gas: Catalytic Reactions of CO and H_2*. **1983**. *2*; D. Reidel Publishing Company: Dordrecht, Holland.
(6) Pruett, R. L. Industrial organic chemicals through utilization of synthesis gas. *Ann. N. Y. Acad. Sci.* **1977**, *295*, 239-248.
(7) Wender, I. Reactions of synthesis gas. *Fuel Process. Technol.* **1996**, *48*, 189-297.
(8) Muscatello, A. C., Hintze, P. E., Meier, A. J., Bayliss, J. A., Karr, L. J., Paley, M. S., Marone, M. J., Gibson, T. L., Surma, J. M., Mansell, J. M. *et al.* Mars Atmospheric In Situ Resource Utilization Projects at the Kennedy Space Center in *Earth and Space Conference*. (2016).
(9) Muscatello, A. Atmospheric Processing Module for Mars Propellant Production in *Department of Physics and Astronomy Seminar*. (2014).
(10) Meier, A. J., Grashik, M. D., Shah, M. G., Sass, J. P., Bayliss, J. A., Hintze, P. E. & Carro, R. V. Full-Scale CO_2 Freezer Project Developments for Mars Atmospheric Acquisition in *2018 AIAA SPACE and Astronautics Forum and Exposition*. (2018).
(11) Zubrin, R., Frankie, B. & Kito, T. Mars In-Situ Resource Utilization Based on the Reverse Water Gas Shift: Experiments and Mission Applications in *33rd Joint Propulsion Conference and Exhibit*. (1997).
(12) Zubrin, R., Muscatello, T., Birnbaum, B., Caviezel, K. M., Snyder, G. & Berggren, M. Progress in Mars ISRU technology in *40th AIAA Aerospace Sciences Meeting & Exhibit*. (2002).
(13) Daza, Y. A., Kent, R. A., Yung, M. M. & Kuhn, J. N. Carbon dioxide conversion by reverse water gas shift chemical looping on perovskite-type oxides. *Ind. Eng. Chem. Res.* **2014**, *53*, 5828-5837.

(14) Daza, Y. A., Maiti, D., Kent, R. A., Bhethanabotla, V. R. & Kuhn, J. N. Isothermal reverse water gas shift chemical looping on $La_{0.75}Sr_{0.25}Co_{(1-Y)}Fe_YO_3$ perovskite type oxides. *Catal. Tod.* **2015**, *258*, 691-698.
(15) Hare, B. J., Maiti, D., Daza, Y. A., Bhethanabotla, V. R. & Kuhn, J. N. Enhanced CO_2 conversion to CO by silica supported perovskite oxides at low temperatures. *ACS Catal.* **2018**, *8*, 3021-3029.
(16) Wenzel, M. & Rihko-Struckmann, L. Thermodynamic Analysis and Optimization of RWGS Processes for Solar Syngas Production from CO_2. *AIChE J.* **2017**, *63*, 15-22.
(17) Fan, L.-S., Li, F., Wang, F., Tong, A. S., Karri, S. B. R., Findlay, J. G., Knowlton, T. M. & Cocco, R. A. Circulating fluidized bed with moving bed downcomers and gas sealing between reactors. USA patent (2014).
(18) Callaghan, C. A. *Kinetics and Catalysis of the Water-Gas-Shift Reaction: A Microkinetic and Graph Theoretic Approach* Doctor of Philosophy in Chemical Engineering thesis, Worcester Polytechnic Institute, (2006).
(19) Ratnasamy, C. & Wagner, J. P. Water Gas Shift Catalysis. *Catal. Rev.: Sci. Eng.* **2009**, *51*, 325-440.
(20) Le Gal, A., Abanades, S. & Flamant, G. CO_2 and H_2O splitting for thermochemical production of solar fuels using nonstoichiometric ceria and ceria/zirconia solid solutions. *Energy Fuels* **2011**, *25*, 4836-4845.
(21) Galvita, V. V., Poelman, H., Bliznuk, V., Detavernier, C. & Marin, G. B. CeO_2- Modified Fe_2O_3 for CO_2 Utilization via Chemical Looping. *Ind. Eng. Chem. Res.* **2013**, *52*, 8416−8426.
(22) Lapp, J., Davidson, J. H. & Lipiński, W. Efficiency of two-step solar thermochemical non-stoichiometric redox cycles with heat recovery. *Energy* **2012**, *37*, 591-600.
(23) Righter, K., Danielson, L., Martin, A., Pando, K., Sutton, S. & Newville, M. Iron Redox Systematics of Martian Magmas. Report No. JSC-CN-24912, (NASA Johnson Space Center, Houston, TX, United States, 2011).
(24) Galvita, V. V., Poelman, H., Bliznuk, V., Detavernier, C. & Marin, G. B. CeO_2-Modified Fe_2O_3 for CO_2 Utilization via Chemical Looping. *Ind. Eng. Chem. Res.* **2013**, *52*, 8416-8426.
(25) Hu, Y. H. *Advances in CO_2 conversion and utilization*. **2010**. *1056*; American Chemical Society: Washington, DC.
(26) Doty, F. D., Doty, G. N., Staab, J. P. & Holte, L. L. Toward efficient reduction of CO_2 to CO for renewable fuels in *4th International Conference on Energy Sustainability*. (2010).
(27) Peña, M. A. & Fierro, J. L. G. Chemical Structures and Performance of Perovskite Oxides. *Chem. Rev.* **2001**, *101*, 1981-2017.
(28) Antoine, O., Bultel, Y. & Durand, R. Oxygen reduction reaction kinetics and mechanism on platinum nanoparticles inside Nafion®. *J. Electroanal. Chem.* **2001**, *499*, 85.
(29) Maiti, D., Hare, B. J., Daza, Y. A., Ramos, A. E., Kuhn, J. N. & Bhethanabotla, V. R. Earth Abundant Perovskite Oxides for Low Temperature CO_2 Conversion. *Energy Environ. Sci.* **2018**, *11*, 648-659.
(30) Evdou, A., Zaspalis, V. & Nalbandian, L. $La_{1-x}Sr_xFeO_{3-\delta}$ perovskites as redox materials for application in a membrane reactor for simultaneous production of pure hydrogen and synthesis gas. *Fuel* **2010**, *89*, 1265-1273.

(31) Jiang, Q., Tong, J., Zhou, G., Jiang, Z., Li, Z. & Li, C. Thermochemical CO_2 splitting reaction with supported $La_xA_{1-x}Fe_yB_{1-y}O_3$ (A = Sr, Cr, B = Co, Mn; $0 \leq x, y \leq 1$) perovskite oxides. *Sol. Energy* **2014**, *103*, 425-437.

(32) Barbero, B. P., Gamboa, J. A. & Cadus, L. E. Synthesis and characterisation of $La_{1-x}Ca_xFeO_3$ perovskite-type oxide catalysts for total oxidation of volatile organic compounds. *Appl. Catal., B* **2006**, *65*, 21.

(33) Bedel, L., Roger, A.-C., Rehspringer, J.-L., Zimmerman, Y. & Kiennemann, A. $La_{(1-y)}Co_{0.4}Fe_{0.6}O_{3-\delta}$ perovskite oxides as catalysts for Fischer–Tropsch synthesis. *J. Catal.* **2005**, *235*, 279.

(34) Demont, A., Abanades, S. & Beche, E. Investigation of Perovskite Structures as Oxygen-Exchange Redox Materials for Hydrogen Production from Thermochemical Two-Step Water-Splitting Cycles. *J. Phys. Chem. C* **2014**, *118*, 12682-12692.

(35) Hernández, W. Y., Tsampas, M. N., Zhao, C., Boreave, A., Bosselet, F. & Vernoux, P. La/Sr-based perovskites as soot oxidation catalysts for Gasoline Particulate Filters. *Catal. Today* **2015**, *258*, 525-534.

(36) Huang, K., Lee, H. Y. & Goodenough, J. B. Sr- and Ni- Doped $LaCoO_3$ and $LaFeO_3$ Perovskites: New Cathode Materials for Solid-Oxide Fuel Cells. *J. Electrochem. Soc.* **1998**, *145*, 3220.

(37) Carter, S., Selcuk, A., Chater, R. J., Kajada, J., Kilner, J. A. & Steele, B. C. H. Oxygen transport in selected nonstoichiometric perovskite-structure oxides. *Solid State Ionics* **1992**, *53-56*, 597.

(38) Galinksy, N., Mishra, A., Zhang, J. & Li, F. $Ca_{1-x}A_xMnO_3$ (A=Sr and Ba) perovskite based oxygen carriers for chemical looping with oxygen uncoupling (CLOU). *Appl. Energy* **2015**, *157*, 358-367.

(39) Sarshar, Z., Kleitz, F. & Kaliaguine, S. Novel oxygen carriers for chemical looping combustion: $La_{1-x}Ce_xBO_3$ (B=Co, Mn) perovskites synthesized by reactive grinding and nanocasting. *Energy Environ. Sci.* **2011**, *4*, 4258-4269.

(40) Alonso, J. A., Martínez-Lope, M. J., Casais, M. T., MacManus-Driscoll, J. L., Silva, P. S. I. P. N. d., Cohen, L. F. & Fernández-Díaz, M. T. Non-stoichiometry, structural defects and properties of $LaMnO_{3+\delta}$ with high δ values ($0.11 \leq \delta \leq 0.29$). *J. Mater. Chem.* **1997**, *7*, 2139-2144.

(41) Najjar, H. & Batis, H. Development of Mn-based perovskite materials: Chemical structure and applications. *Catal. Rev.: Sci. Eng.* **2016**, *58*, 371-348.

(42) Nachon, M., Clegg, S. M., Mangold, N., Schröder, S., Kah, L. C., Dromart, G., Ollila, A., Johnson, J. R., Oehler, D. Z., Bridges, J. C. *et al.* Calcium sulfate veins characterized by ChemCam/Curiosity at Gale crater, Mars. *J. Geophys. Res.: Planets* **2014**, *119*, 1991-2016.

(43) Boynton, W. V., Ming, D. W., Kounaves, S. P., Young, S. M. M., Arvidson, R. E., Hecht, M. H., Hoffman, J., Niles, P. B., Hamara, D. K., Quinn, R. C. *et al.* Evidence for Calcium Carbonate at the Mars Phoenix Landing Site. *Science* **2009**, *325*, 61-64.

(44) Lanza, N. L., Fischer, W. W., Wiens, R. C., Grotzinger, J., Ollila, A. M., Cousin, A., Anderson, R. B., Clark, B. C., Gellert, R., Mangold, N. *et al.* High manganese concentrations in rocks at Gale Crater, Mars. *Geophys. Res. Lett.* **2014**, *41*, 5755-5763.

(45) Predoana, L., Malic, B., Kosec, M., Carata, M., Caldararu, M. & Zaharescu, M. Characterization of $LaCoO_3$ powders obtained by water-based sol-gel method with citric acid. *J. Eur. Ceram. Soc.* **2007**, *27*, 4407-4411.

(46) Popa, M. & Kakihana, M. Synthesis of lanthanum cobaltite ($LaCoO_3$) by the polymerizable complex route. *Solid State Ionics* **2002**, *151*, 251-257.

(47) Berndt, U., Maier, D. & Keller, C. New $A^{III}B^{III}O_3$ Interlanthanide Perovskite Compounds. *J. Solid State Chem.* **1975**, *13*, 131-135.

(48) Coates, R. V. & McMillan, J. W. Oxygen deficiency in perovskite-type compounds of calcium. *J. Appl. Chem.* **1964**, *14*, 346-350.

(49) Marezio, M., Remeika, J. P. & Dernier, P. D. The crystal chemistry of the rare earth orthoferrites. *Acta Crystallogr., Sect. B: Struct. Crystallogr. Cryst. Chem.* **1970**, *26*, 2008-2022.

(50) Grier, D. & McCarthy, G. ICDD Grant-in-Aid. (North Dakota State Univ., Fargo, ND, USA, 1994).

(51) Hohenberg, P. & Kohn, W. Inhomogeneous Electron Gas. *Phys. Rev.* **1964**, *136*, B864-B871.

(52) Kohn, W. & Sham, L. J. Self-Consistent Equations Including Exchange and Correlation Effects. *Phys. Rev.* **1965**, *140*, A1133-A1138.

(53) Kresse, G. & Furthmüller, J. Efficient iterative schemes for *ab initio* total-energy calculations using a plane-wave basis set. *Phys. Rev. B.* **1996**, *54*, 11169-11186.

(54) Kresse, G. & Joubert, D. From ultrasoft pseudopotentials to the projector augmented-wave method. **1999**, *59*, 1758-1775.

(55) Kresse, G. & Hafner, J. *Ab initio* molecular dynamics for liquid metals. *Phys. Rev. B.* **1993**, *47*, 558-561.

(56) Perdew, J. P., Burke, K. & Ernzerhof, M. Generalized Gradient Approximation Made Simple. *Phys. Rev. Lett.* **1996**, *77*, 3865-3868.

(57) Monkhorst, H. J. & Pack, J. D. Special points for Brillouin-zone integrations. *Phys. Rev. B* **1976**, *13*, 5188-5192.

(58) Wang, L., Maxisch, T. & Ceder, G. Oxidation energies of transition metal oxides within the GGA + U framework. *Phys. Rev. B* **2006**, *73*, 195107.

(59) Maiti, D., Daza, Y. A., Yung, M. M., Kuhn, J. N. & Bhethanabotla, V. R. Oxygen vacancy formation characteristics in the bulk and across different surface terminations of $La_{(1-x)}Sr_xFe_{(1-y)}Co_yO_{(3-\delta)}$ perovskite oxides for CO_2 conversion. *J. Mater. Chem. A* **2016**, *4*, 5137-5148.

(60) Cooper, T., Scheffe, J. R., Galvez, M. E., Jacot, R., Patzke, G. & Steinfeld, A. Lanthanum Manganite Perovskites with Ca/Sr A-site and Al B-site Doping as Effective Oxygen Exchange Materials for Solar Thermochemical Fuel Production. *Energy Technol.* **2015**, *3*, 1130-1142.

(61) Dey, S. & Rao, C. Splitting of CO2 by manganite perovskites to generate CO by solar isothermal redox cycling. *ACS Energy Letters* **2016**, *1*, 237-243.

(62) Nair, M. M. & Abanades, S. Experimental screening of perovskite oxides as efficient redox materials for solar thermochemical CO_2 conversion. *Sustainable Energy Fuels* **2018**, *2*, 843-854.

(63) Daza, Y. A., Maiti, D., Hare, B. J., Bhethanabotla, V. R. & Kuhn, J. N. More Cu, more problems: Decreased CO_2 conversion ability by Cu-doped $La_{0.75}Sr_{0.25}FeO_3$ perovskite oxides. *Surf. Sci.* **2016**, *648*, 92-99.

(64) Hayashi, H., Inaba, H., Matsuyama, M., Lan, N. G. & Dokiya, M. Structural consideration on the ionic conductivity of perovskite-type oxides. *Solid State Ionics* **1999**, *122*, 1-15.

(65) Sammells, A. F., Cook, R. L., White, J. H., Osborne, J. J. & MacDuff, R. C. Rational selection of advanced solid electrolytes for intermediate temperature fuel cells. *Solid State Ionics* **1992**, *52*, 111-123.

(66) Cherry, M., Islam, M. S. & Catlow, C. R. A. Oxygen Ion Migration in Perovskite-Type Oxides. *J. Solid State Chem.* **1995**, *118*, 125-132.

(67) Diethelm, S., Van-herle, J., Sfeir, J. & Buffat, P. Correlation between oxygen transport properties and microstructure in $La_{0.5}Sr_{0.5}FeO_{3-\delta}$. *J. Eur. Ceram. Soc.* **2005**, *25*, 2191-2196.

(68) Etchegoyen, G., Chartier, T., Julian, A. & Del-Gallo, P. Microstructure and oxygen permeability of a $La_{0.6}Sr_{0.4}Fe_{0.9}Ga_{0.1}O_{3-\delta}$ membrane containing magnesia as dispersed second phase particles. *J. Membr. Sci.* **2006**, *268*, 86-95.

(69) Shannon, R. D. Revised effective ionic radii and systematic studies of Interatomic distances in halides and chalcogenides. *Acta Cryst.* **1976**, *A32*, 751-767.

(70) Ciambelli, P., Cimino, S., Lisi, L., Faticanti, M., Minelli, G., Pettiti, I. & Porta, P. La, Ca, Fe oxide perovskites: preparation, characterization and catalytic properties for methane combustion. *Appl. Catal., B* **2001**, *33*, 193-203.

(71) Hare, B. J., Maiti, D., Ramani, S., Ramos, A. E. & Bhethanabotla, V. R. Thermochemical conversion of carbon dioxide by reverse water-gas shift chemical looping using supported perovskite oxides. *Catal. Tod.* **2019**, *323*, 225-232.

(72) Kuhn, J. N. & Ozkan, U. S. Surface properties of Sr- and Co-doped $LaFeO_3$. *J. Catal.* **2008**, *253*, 200-211.

(73) Druce, J., Tellez, H., Burriel, M., Sharp, M., Fawcett, L., Cook, S., McPhail, D., Ishihara, T., Brongersma, H. & Kilner, J. Surface termination and subsurface restructuring of perovskite-based solid oxide electrode materials. *Energy Environ. Sci.* **2014**, *7*, 3593-3599.

(74) *Thermo Scientific Avantage Data System for XPS*, <https://xpssimplified.com/periodictable.php> (2019).

(75) Milt, V. G., Spretz, R., Ulla, M. A., Lombardo, E. A. & Fierro, J. L. G. The nature of active sites for the oxidation of methane on La-based perovskites. *Catal. Lett.* **1996**, *42*, 57-63.

(76) Islam, M. S. Ionic transport in ABO_3 perovskite oxides: a computer modelling tour. *J. Mater. Chem.* **2000**, *10*, 1027-1038.

(77) Luo, C., Zheng, Y., Ding, N., Wu, Q., Bian, G. & Zheng, C. Development and Performance of CaO/La_2O_3 Sorbents during Calcium Looping Cycles for CO_2 Capture. *Ind. Eng. Chem. Res.* **2010**, *49*, 11778-11784.

(78) Richter, J., Braun, A., Harvey, A. S., Holtappels, P., Graule, T. & Gauckler, L. J. Valence changes of manganese and praseodymium in $Pr_{1-x}Sr_xMn_{1-y}In_yO_{3-\delta}$ perovskites upon cation substitution as determined with XANES and ELNES. *Physica B* **2008**, *403*, 87-94.

(79) Shirsat, A. N., Ali, M., Kaimal, K. N. G., Bharadwaj, S. R. & Das, D. Thermochemistry of $La_2O_2CO_3$ decomposition. *Thermochim. Acta* **2003**, *399*, 167-170.

(80) Pisecny, P., Husekova, K., Frohlich, K., Harmatha, L., Soltys, J., Machajdik, D., Espinos, J. P., Jergel, M. & Jakabovic, J. Growth of lanthanum ocide films for application as a gate dielectric in CMOS technology. *Mater. Sci. Semicond. Process.* **2004**, *7*, 231-236.

(81) Albrecht, K. O., Wagenbach, K. S., Satrio, J. A., Shanks, B. H. & Wheelock, T. D. Development of a CaO-Based CO_2 Sorbent with Improved Cyclic Stability. *Ind. Eng. Chem. Res.* **2008**, *47*, 7841-7848.

(82) Wagman, D. D., Kilpatrick, J. E., Taylor, W. J., Pitzer, K. S. & Rossini, F. D. Heats, free energies, and equilibrium constants of some reactions involving O_2, H_2, H_2O, C, CO, CO_2, and CH_4. *J. Res. Natl. Bur. Stand.* **1945**, *34*, 143-161.

(83) Chowdhury, M. B. I., Quddus, M. R. & deLasa, H. I. CO_2 capture with a novel solid fluidizable sorbent: Thermodynamics and Temperature Programmed Carbonation–Decarbonation. *Chem. Eng. J.* **2013**, *232*, 139-148.

(84) Scheffe, J. R., Weibel, D. & Steinfeld, A. Lanthanum-Strontium-Manganese Perovskites as Redox Materials for Solar Thermochemical Splitting of H_2O and CO_2. *Energy Fuels* **2013**, *27*, 4250-4257.

Abstract Graphic